Oil-Spill-Response-Oriented Information Products Derived From a Rapid-Repeat Time Series of SAR Images

Martine M. Espeseth, Cathleen E. Jones, *Member, IEEE*, Benjamin Holt, *Member, IEEE*, Camilla Brekke, *Member, IEEE*, and Stine Skrunes, *Member, IEEE*

***Abstract*—New quantitative and semiautomated methods for analyzing oil slick evolution using a time series of L-band synthetic aperture radar (SAR) images with short repeat time are developed and explored. In this study, two methods that are complementary in terms of identifying temporal changes within an oil slick are presented. The two methods reflect two ways of evaluating the oil slicks. The first method identifies regions within the slick that show persistently high damping ratio (the contrast between clean sea and oil intensity), using higher damping values as a proxy for increasing oil thickness. This method also weights the age of the scenes as the algorithm incorporates new images. The second method outputs the short-term drift pattern and the changes in the damping ratios and copolarization ratios between two scenes, proxies for thickness, and emulsification. Both methods can aid in identifying regions of high priority for oil recovery. Due to the simplicity of the methods, they can be adapted to time-series data from different types of sensors, e.g., optical and SAR imagery. The methods are demonstrated on three L-band uninhabited aerial vehicle SAR UAVSAR time series acquired in November 2016 over a persistent seep in the Mississippi Canyon Block 20 of the Gulf of Mexico. The results of the two methods clearly show the movement and the weathering of the oil as a function of both time and location.**

***Index Terms*—Copolarization ratio, damping ratio, oil spill, oil spill response, polarimetry, synthetic aperture radar (SAR), uninhabited aerial vehicle synthetic aperture radar (UAVSAR).**

I. Introduction

SYNTHETIC aperture radar (SAR) instruments are a key operational monitoring tool for detection of marine oil spills. Most commonly, a single SAR image is used to identify location, extent, and, if possible, the source of the spill. This information is often available in oil spill detection reports from operational services. Tools for quantifying the oil's characteristics and identifying their variations within a slick are still limited within operational systems. Within the research community, studies using a single SAR scene have demonstrated the potential to characterize physical properties within oil slicks, specifically the thickness and the volumetric fraction of oil [1]–[9]. Studies have observed that thicker oil, including weathered emulsified oil, causes more damping of the capillary and short gravity waves and thus appears darker in SAR than thinner oil layers (e.g., sheen) [3], [10]–[12]. With this information available, it is possible to detect actionable oil in an operational response setting.

A single SAR scene is valuable when obtaining a snapshot view of an oil spill. Tracking the evolution of a slick requires several images of the same slick, i.e., one must integrate scenes from several SAR sensors or repeat imaging with one sensor. The use of multiple SAR/optical images covering an oil spill/seep has proven to be very useful for extracting information about the drift pattern and the oil extent, two important factors that can aid in assessing the potential environmental impacts from such hazards. For example, both optical and SAR time series with a long revisit time (days/weeks) have been investigated [13]–[15].

An airborne SAR sensor can provide rapid repeat images to monitor how the slick drifts and weathers on the sea surface. In this study, we consider how a series of SAR images acquired with short revisit time (minutes to hours) can be used to identify areas within oil slicks of relatively thicker or more persistent oil and their short-term drift patterns. This study introduces complementary information products that could be valuable in the recovery process, where timely knowledge of the spill is important. We demonstrate that combining the temporal aspect, using multiple SAR images with short repeat times, with characterization of an oil spill can provide new information to improve decision making during clean-up.

Studies with short repeat time series using SAR images have demonstrated the potential of using the damping ratio to extract information about the transport, evolution, and change in SAR properties on a short time scale (see [11] and [16]). The methodologies presented in this study are aimed at creating map products that combine all of this information to quantify and visually depict the temporal evolution of the slick in an easily understandable representation.

Manuscript received October 29, 2019; revised January 27, 2020, April 1, 2020, and May 15, 2020; accepted June 4, 2020. Date of publication June 19, 2020; date of current version July 2, 2020. This work was funded by the Centre for Integrated Remote Sensing and Forecasting for Arctic Operations under RCN Grant 237906. This research was carried out in part at the Jet Propulsion Laboratory, California Institute of Technology, under contract with the National Aeronautics and Space Administration (Task Order NNN13D788T). *(Corresponding author: Martine M. Espeseth.)*

Martine M. Espeseth, Camilla Brekke, and Stine Skrunes are with the Department of Physics and Technology, UiT The Arctic University of Norway, 9037 Tromsø, Norway (e-mail: martine.espeseth@uit.no; camilla.brekke@uit.no; stine.skrunes@uit.no).

Cathleen E. Jones and Benjamin Holt are with the Jet Propulsion Laboratory, California Institute of Technology, Pasadena, CA 91125 USA (e-mail: cathleen.e.jones@jpl.nasa.gov; benjamin.m.holt@jpl.nasa.gov).

Digital Object Identifier 10.1109/JSTARS.2020.3003686

From an oil spill response perspective, the first step in making a map usable by responders is to identify the oil slick using either manual or automatic segmentation algorithms. The purpose of this study is to take the next steps, namely: 1) developing methods for automatically identifying regions with persistent presence of thick oil, indicated by high damping over a period of time; and 2) extracting information about the oil slick drift pattern to show where the thicker oil is moving. Such information can be used as input to improve the oil spill response and clean-up process by reducing reliance on visual analysis, which can lead to limited, biased, or subjective conclusions. The analysis is conducted on three-time series, each consisting of between six and nine uninhabited aerial vehicle synthetic aperture radar (UAVSAR) scenes, covering a persistent oil seep in the Gulf of Mexico. This area is used as the test case for demonstrating the potential of the suggested methods because the slick formed from the seep often exhibits variations in oil properties within the slick (see, e.g., [11] and [17]).

II. Selected SAR Features

A number of features extracted from quad-polarimetric SAR products have been investigated for their ability to both detect and characterize oil (see, e.g., [5], [6], [9], and [18]). For daily monitoring, the single-polarization (one polarization channel) or the conventional dual-polarization (one linear co- and cross-polarization channel) SAR mode is preferred over the quad-polarimetric mode (four polarization channels) due to its typically larger image swath. However, using the single- or dual-polarization SAR comes at a cost of less polarimetric information, which might result in limitations when, for example, attempting to characterize the oil slicks. In a response situation, where the oil spill location is already known, multipolarization and high spatial resolution are more important than large spatial coverage.

The two main physical factors impacting the interaction between the incoming radar signal and the surface oil are the dielectric properties and the roughness of the scattering surface. In open water, the small-scale roughness induced by the wind is higher in the surrounding clean sea compared to the oil-covered area due to the oil damping of the capillary and short gravity waves. The dielectric permittivity of seawater is much higher than that of oil. For a thin oil layer, the oil dielectric properties do not affect the backscatter amplitude in a measurable way, but if the oil slick is thick (centimeter) or there is high concentration of oil in the oil/sea mixture, the dielectric properties observed by the radar may be altered by the presence of oil. SAR instruments measure only the response from the upper surface, not in the water column, due to little penetration of microwaves into seawater. Hence, the oil droplets located in the water column will not be detected by SAR.

We have selected two features that can be related to roughness and the dielectric property. The first feature is the contrast between the VV (vertical transmit and vertical receive) intensity in clean sea versus oil, named the damping ratio ($\mathrm{DR}_{\mathrm{VV}}$) (see [2]) and the second is the copolarization ratio contrast (CPR_c). The reasons for selecting these particular features are discussed in Sections II-A and II-B.

The selected features are defined as

$$\mathrm{DR}_{\mathrm{VV}}(\theta) = \sigma^{0,\mathrm{sea}}_{\mathrm{VV}}(\theta)/\sigma^{0}_{\mathrm{VV}}(\theta) \tag{1}$$

$$\mathrm{CPR}_c(\theta) = \left(\frac{\sigma^0_{\mathrm{HH}}(\theta)}{\sigma^0_{\mathrm{VV}}(\theta)}\right)^{\mathrm{sea}} \Bigg/ \left(\frac{\sigma^0_{\mathrm{HH}}(\theta)}{\sigma^0_{\mathrm{VV}}(\theta)}\right). \tag{2}$$

Here, σ^0_{VV} is the radar cross section (σ^0) in VV polarization, θ is the incidence angle, and $\sigma^{0,\mathrm{sea}}_{\mathrm{VV}}$ is the radar cross section from the clean sea surrounding the oil slick. Following the established literature, the damping ratio is calculated as the inverse of the ratio of the pixel value to the clean sea pixel value for the same incidence angle. The copolarization ratio (CPR) is the ratio of the HH- (horizontal transmit and horizontal receive) and VV-intensity, and the contrast is calculated as the inverse ratio to the clean sea values, consistent with the damping ratio formula, and given the abbreviation CPR_c. The reason is that the marine surface oil investigated in this study spans a significant range of incidence angles, thereby introducing an incidence angle dependence for this feature across the oil slick. Taking the ratio of an area covering clean sea and oil for a given feature (e.g., CPR) partially cancels this dependence, especially if the incidence angle offsets between clean sea and oil are minor. The VV return is in general higher than the HH return for ocean features, thereby producing CPR values between 0 and 1. $\mathrm{DR}_{\mathrm{VV}}$ can be extracted from a single-polarimetric SAR system, where only the VV channel is needed. CPR_c needs a dual-polarimetric system with HH and VV capabilities (such as those carried by TerraSAR-X and the Radarsat Constellation Mission).

A. VV-Damping Ratio

The damping ratio has been observed to show a high contrast between oil and clean sea. According to the Bragg scattering theory, the damping ratio is a measure of the difference in spectral energy density of the ocean surface waves between oil-free and oil-covered surfaces [10]. The damping ratio has been shown to be sensitive to relative thickness variations within mineral oil slicks, where thicker oil causes more damping of the capillary and short gravity waves [3], [10]–[12]. Gade *et al.* [2] determined that the damping ratio increased with increasing Bragg wavenumber and observed that L-band SAR measured a lower damping ratio compared to C- and X-band SAR at the same incidence angle. Under specific environmental conditions (wind speed approximately 5–6 m/s), an early study [19] also observed that a significant reduction in backscatter was correlated with the thickest parts of the oil. A recent study [20] based on a laboratory experiment using oil emulsion and crude oil with different thicknesses demonstrated that the damping ratio increased with oil thickness (using X- to Ka-band radars), but reached a maximum damping ratio value at a given oil thickness threshold at 1–2 mm for oil emulsion. Higher damping was also reported for crude oil compared to emulsified oil in [20]. Airborne measurements and cruise surveys near the Mississippi Canyon Block 20 (MC-20) slick (the same oil slick studied here) reported oil thickness in the range 0.04 μm to 1 mm (sheen to

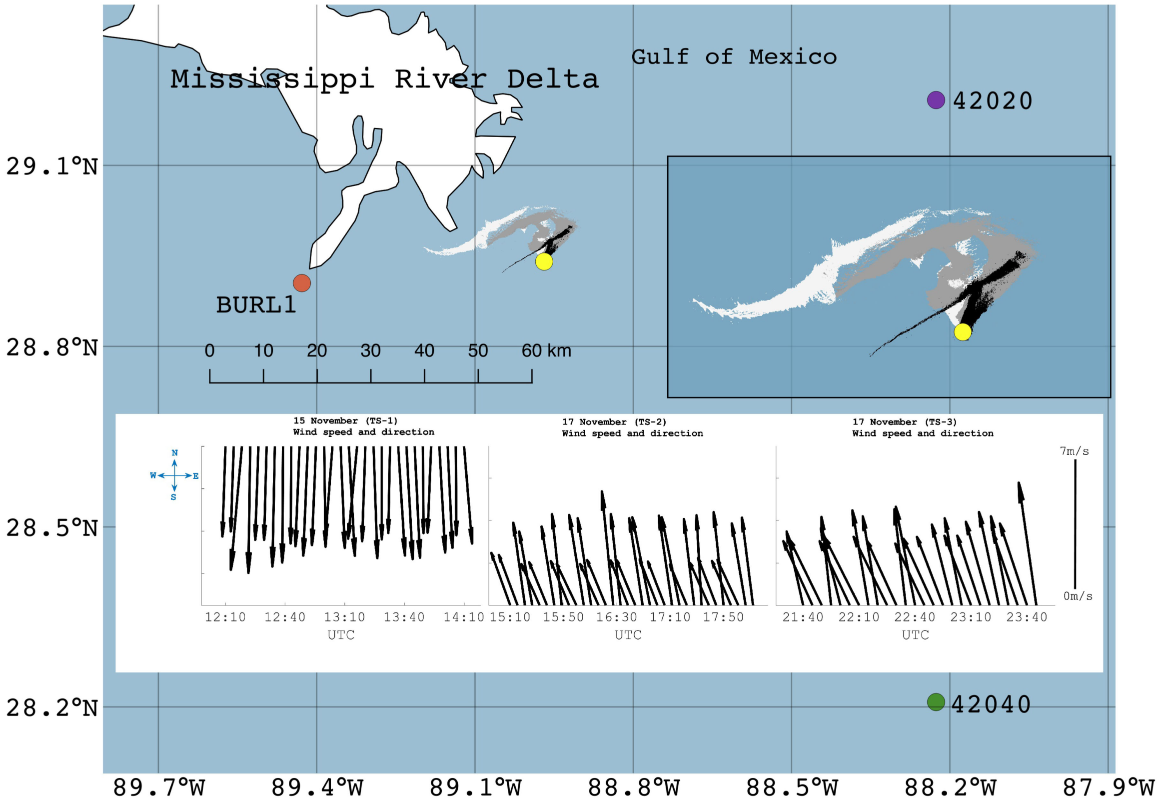

Fig. 1. Study area and the oil slick area covered by the UAVSAR. Wind information is collected from the NOAA BURL1 station (orange circle), NOAA buoy 42020 (purple circle), and NOAA buoy 42040 (green circle). The yellow circle shows the location of the persistent seep in MC-20 (see, e.g., [11] and [14]). The three different tones of gray show the coverage of the joint oil slick masks from the segmentation of the total set of scenes from TS-1, TS-2, and TS-3 (from dark to light, respectively). The panel shows the evolution of the wind vectors from three buoys measured during the time period of the three sets of UAVSAR data. The wind velocities are converted to U10.

crude oil) [11], [13], [21]. As described in [13] and [21] and other studies regarding this site, there is considerable patchiness within the oil slicks in this region, ranging from rainbow sheen to fresh oil and emulsions, with the thicker components covering the smaller areas within the larger slicks. Based on the experiment presented in [20], the damping ratio studied here will, most likely, increase with oil thickness. The damping ratio has been used in several oil spill studies to identify internal zones [3], [11], [22], to extract the volumetric mixing ratio of oil in water [6], and to identify areas containing thicker oil within a slick [12]. The VV channel is used when calculating the damping ratio in preference to the HH and HV channels because VV provides higher contrast between oil and clean sea and is less affected by the system noise [1], [23], [24].

B. Copolarization Ratio

According to the tilted Bragg scattering model [25], the ratio of the two intensities HH and VV cancels the small-scale surface roughness. This model has been shown to accurately reproduce L-band SAR scattering from oil slicks using two different high-signal-to-noise-ratio (SNR) airborne instruments [5], [9]. The ratio is a function of the relative dielectric properties of the multilayered medium (air, oil, and seawater), incidence angle, and the geometry of the ocean surface waves [25]. To obtain a high oil-to-sea contrast with this feature, the relative dielectric properties must be altered by the oil. This means that the oil layer thickness must be comparable to the penetration depth[1] of the radar (order of mm for L-band), so that the backscattered signal comes from the oil layer itself. Hence, the CPR might aid in the detection of the thickest oil within a slick [5]. In [5], the authors demonstrated, both theoretically and experimentally using UAVSAR data, that the CPR values were greater across oil-infested areas compared to oil-free areas for incidence angles spanning 30–60°. In this study, CPR$_c$ is used instead of CPR. CPR$_c$ is still a function of the same properties as the CPR, but produces values close to 1 for clean sea areas and less than 1 for oil-infested areas.

III. Study Area and Dataset

This study is based on three-time series of calibrated and multilooked data acquired with the L-band UAVSAR airborne sensor over a three-day period in November 2016. The UAVSAR data are openly available from the Alaska Satellite Facility.[2] The reader is referred to [27] for a more detailed description of the calibration of the UAVSAR. The advantages of using the UAVSAR sensor are the fine resolution (approximately 2.5×1 m range and azimuth single look resolution), the high SNR [27],

[1]The penetration depth is defined as the depth at which the radar signal is attenuated to $1/e$ [26].

[2]Online. [Available]: http://www.asf.alaska.edu

TABLE I
OVERVIEW OF THE ACQUISITION PERIOD AND THE NUMBER OF ACQUISITIONS IN EACH TIME SERIES

Time series ID	Date	Time period (UTC)	Number of scenes	Time between acquisition (min)
TS-1	15 Nov.	12:12-14:25	8	18-20
TS-2	17 Nov.	15:10-17:48	9	19-21
TS-3	17 Nov.	21:58-23:47	6	19-25

and the possibility of short repeat time between scenes. The three time series covered an area of MC-20 in the Gulf of Mexico, where there has been a persistent oil seep of light Louisiana sweet crude oil since 2004 [13], [14], [28], [29] (see Fig. 1). This spill is well known and has been investigated in several previous studies (see, e.g., [11], [13]–[15], [21], [28], and [30]).

One study [13] observed that the average slick area is approximately 14 km^2 per image (evident from both SAR and optical imagery) and with an estimated oil discharge rate of 48–1700 barrels/day. Another study, [15], observed on average 2.7 $\pm$ 2.4 km^2 per day using 42 TerraSAR-X scenes. The oil originates from the seafloor, which lies at a depth of 150 m in this location (MC-20) [14] and rises to the surface after undergoing different phases such as the plume phase and the post-terminal phase (see e.g., [31], [32], and references therein). The oil leaking from the seafloor might also start to diffuse or disperse when traveling toward the surface. After reaching the surface, the oil will continue to weather and move as a result of the ocean and wind conditions. Furthermore, this persistent oil slick in MC-20 travels along the isobaths (generally southwest to northeast) [30]. The drift and extent are largely being controlled by the river dynamics, and the oil pathway aligned with the riverfront [13], [14].

Table I contains information about the acquisition period and the number of acquisitions within each time series. The first time series (TS-1) was acquired on November 15, 2016, the second time series (TS-2) was acquired two days later in the morning (local time) on November 17, and the third time series (TS-3) was acquired in the afternoon (local time) on November 17. The scenes were acquired approximately 20 min apart. Fig. 1 shows the study area and the slick extent in the three time series displayed in different tones of gray. The three time series were acquired under various wind and ocean conditions, as shown in the panel of Fig. 1.

Wind information is obtained from three buoys located around the study site (see Fig. 1). The NOAA BURL1 station is located approximately 45 km from the seep in MC-20 with an anemometer height of 38 m. The other two buoys (buoy 42020 and buoy 42040) have an anemometer height of 4 m and are located approximately 78 and 110 km from the site. The wind speed has been converted to equivalent neutral wind with an anemometer height of 10 m (U10) [33], which resulted in a change of approximately $\pm$1 m/s. The panels in Fig. 1 show the wind vectors concurrent with each time series. The wind directions were relatively consistent within each time series, and the measured wind speeds from the two days, 3.8–6.6 m/s, are within the theoretical range (2–3 m/s to 10–14 m/s), where oil spill detection is possible [34], [35]. The wind directions are all orientated toward the south for the time period of TS-1, with a small westward component. On November 17, the wind directions were toward the north to northwest across the time period of TS-2 and TS-3.

A. Oil Slick Masks

The oil slick masks were obtained from the UAVSAR data by applying a Gaussian Mixture model to DR_{VV} (see [36] for a thorough description of this unsupervised segmentation method). The output segments from this method are labeled as oil-free or oil-infested segments, resulting in a binary image, which was filtered using a connectivity filter to reduce the grainy patterns that result from radar speckle.

The slick masks for the scenes within one time series vary due to transport, spreading, and weathering processes. Therefore, all the individual masks are joined to form a new overall mask, which covers the entire oil slick extent across the given time series. The UAVSAR data are provided in several formats, and we use the UAVSAR scenes that have been multilooked to a pixel spacing of 5 $\times$ 7.2 m (slant range $\times$ azimuth). Then, we calculated DR_{VV} and CPR_c and generated the oil masks. Finally, DR_{VV}, CPR_c, and oil masks were georeferenced[3] creating a stack of UAVSAR scenes on the same latitude/longitude grid (see Figs. 2–4).

To simplify the discussion, the slicks are divided into regions, indicated by the red boxes. The look direction is toward the left of the flight direction, and three flight directions were used in the data collection of TS-1, which are indicated by labels FD_1, FD_2, and FD_3 in Fig. 2. This results in a slightly different incidence angle range across the slick; flight ID 001 had incidence angles spanning 44–52°; flight ID 002 and 003 had incidence angles spanning 50–55°, and the remaining flights (flight ID 004–008) had incidence angles spanning 46–52° across the slick. Since all the flights were looking close to downwind, the effect on the look direction and the small incidence angle variations among the scenes (in TS-1) is small. Only one flight direction (FD_3) was used in the acquisition of the scenes in TS-2 and TS-3, and the incidence angles span approximately 40° $\pm$ 15° across the oil slicks. The flights in TS-2 and TS-3 were looking upwind. TS-2 and TS-3 were acquired under approximately the same imaging geometry, resulting in less deviation between the features investigated due to incidence angle variations and different look direction. In addition, the two features are calculated with respect to the clean sea, which reduces the incidence angle variations across the oil slick and between the scenes (see Section II).

B. Short Time Area Evolution of the Persistent Seep

The estimated area from the segmentation masks varies from 2 to 35 km^2, where the smallest areas are observed on November 15 (TS-1), and the larger areas are observed on November 17 (see Fig. 5). This matches [13], where an average of 14 km^2 per image was found across the three-time series. The estimated slick areas for all scenes within a time series (spanning approximately

[3]Georeferenced using WGS84 and EPSG:4326.

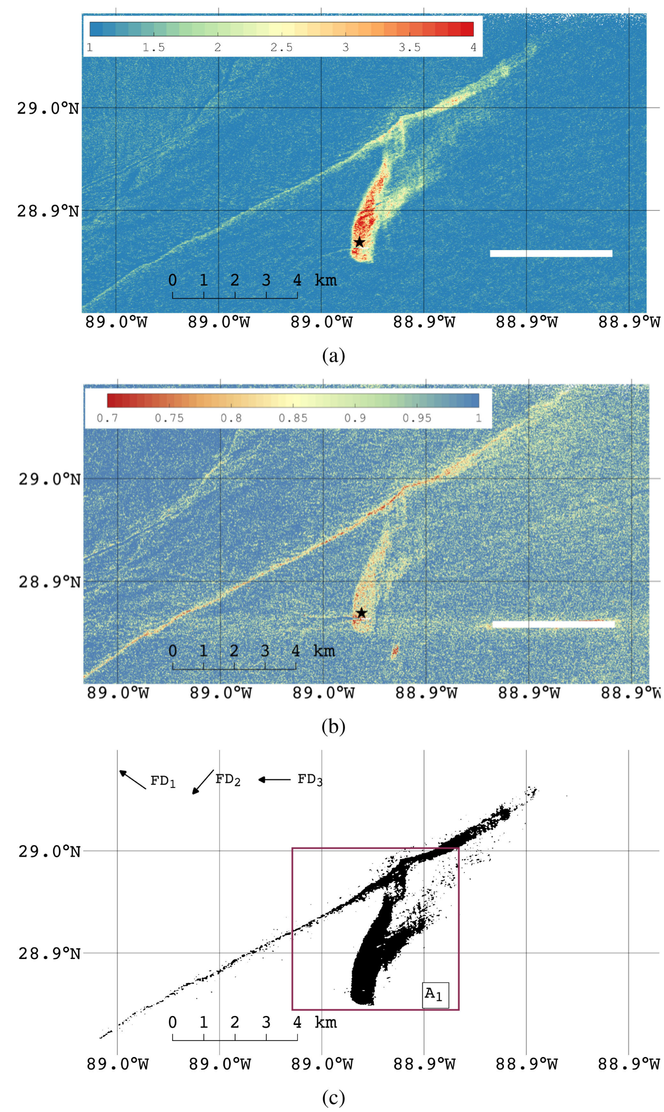

Fig. 2. (a) VV damping ratio (DR_{VV}), (b) the copolarization ratio contrast (CPR_c), and (c) the corresponding mask of the clean sea (background) and oil-infested areas (black) from the TS-1 scene acquired at 13:09 UTC. The imaging direction of UAVSAR is to the left of the flight direction (FD). The sidelobes from the point target to the lower right is masked out. The black star is the approximate location of the seep (see, e.g., [11] and [14]).

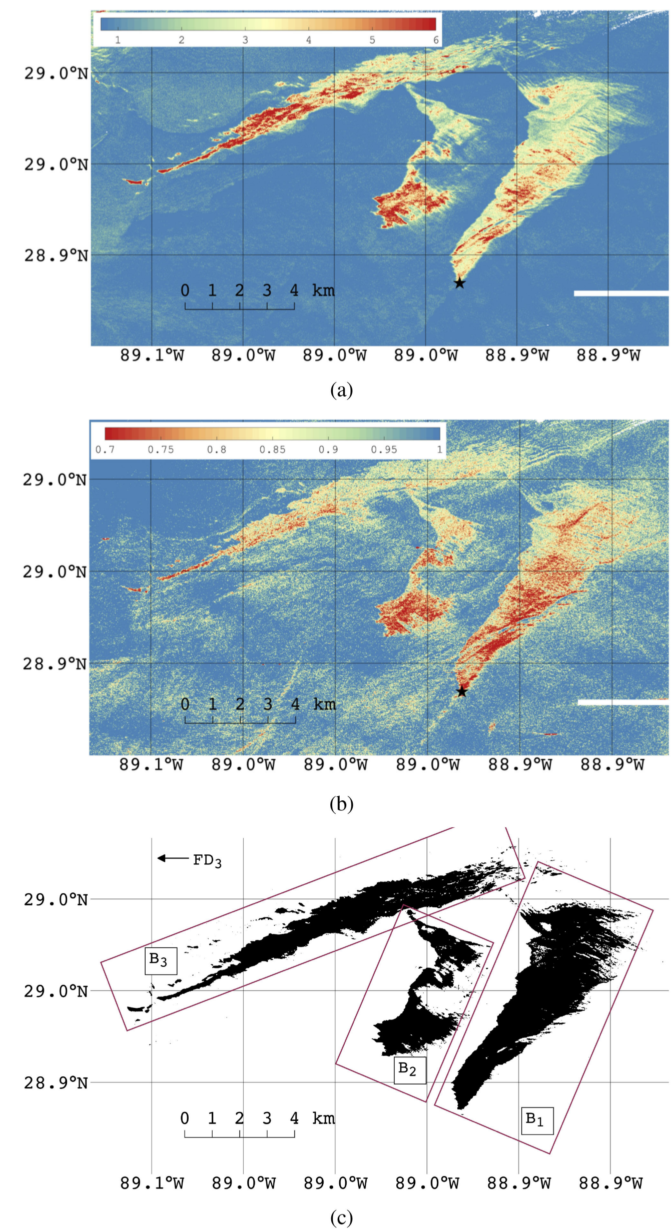

Fig. 3. (a) VV damping ratio (DR_{VV}), (b) the copolarization ratio contrast (CPR_c), and (c) the corresponding mask of the clean sea (background) and oil-infested areas (black) from the TS-2 scene acquired at 16:11 UTC. See Fig. 2 caption for more labeling details.

2–4 h) are similar. Hence, the total area does not change drastically over these short time series, which might allow identification of stable areas with approximately the same SAR backscatter intensity over time. The reasons why there are changes in the area across 15 November (TS-1) and 17 November (TS-2 and TS-3) are most likely due to changes in wind, current, and/or rate of the oil discharge from the sea floor.

IV. Method

We are interested in identifying temporal changes in the investigated features that can be used to observe short-term oil slick drift. These changes are connected to the spreading and weathering processes of the oil slick, and are reflected in the backscattered signal. The damping ratio and copolarization ratio extracted from SAR have been frequently used in single scene analysis, and we want to demonstrate some examples of how these features can be used in a time series. Therefore, the changes in investigated feature values are explored as a function of time at various locations within the slick. By quantifying the change in the parameters, we can obtain information about the *stability* of the SAR features in the oil slick as a function of time. Here, the stability is used as a measure of how little a feature value changes within a given area over a certain time interval. Different products derived from statistical analysis are used to evaluate whether a time series with short repeat time can provide complementary information to a single acquisition.

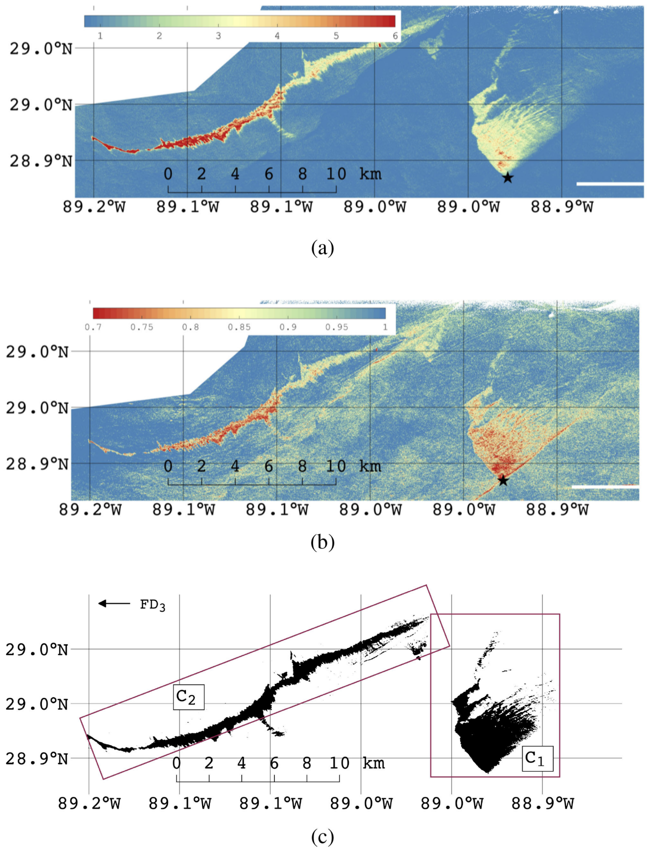

Fig. 4. (a) VV damping ratio (DR_{VV}), (b) the copolarization ratio contrast (CPR_c), and (c) the corresponding mask of the clean sea (background) and oil-infested areas (black) from the TS-3 scene acquired at 23:27 UTC. See Fig. 2 caption for more labeling details.

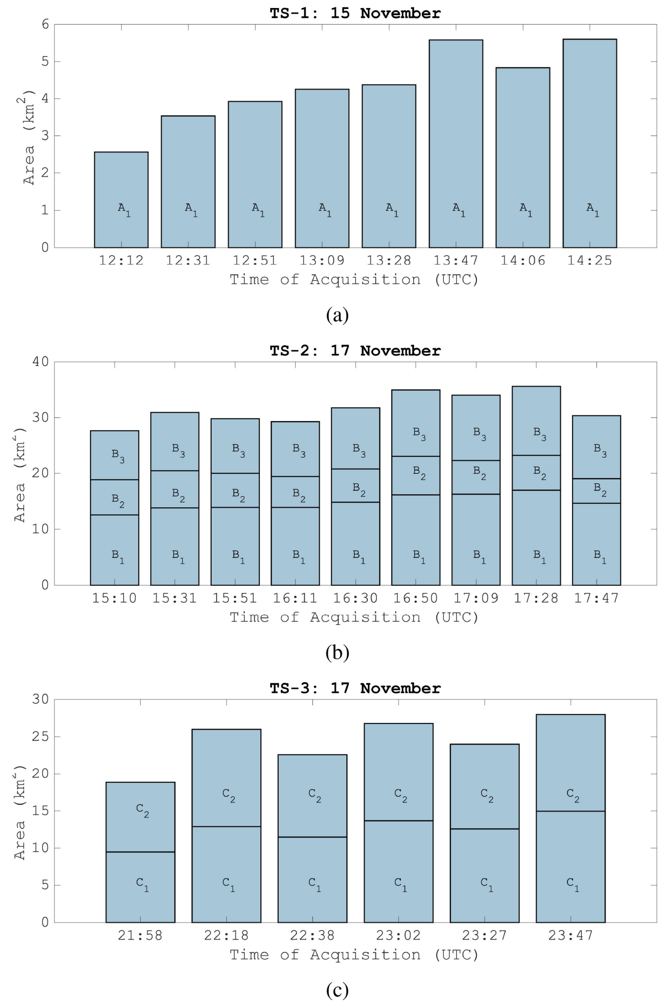

Fig. 5. Estimated area covered by oil from the segmentation masks. Each bar is divided in the regions defined in Figs. 2–4. (a) TS-1. (b) TS-2. (c) TS-3.

One important step in a response action is to investigate the spill site for situational awareness. The mineral oil thickness might vary within the oil slick and create zones with varying characteristics that affect the SAR backscatter signal. Various containment and recovery equipment exist, e.g., mechanical, chemical, biological, and/or physical methods, whose efficiency depends upon the oil thickness. Knowledge of the thicker oil's location and drift pattern could be used to identify locations where the response should be focused. In this study, we explore methods that capture how these zones change as a function of time and quantify the stability of these zones.

A. *Method 1—Detection of Stable Regions Within the Oil Slick*

Method 1 identifies those locations where the VV damping ratio is consistently high throughout the time series. This is achieved by counting the number of scenes in which DR_{VV} for a given pixel is above a certain threshold (T_h). Operationally, the most recent acquisition is the most important scene in a time series, since it provides the latest status of an oil spill. To account for this, the stability level (SL) is calculated by applying higher weights to the more recent scenes. We use an exponentially weighted moving average filter, and the input to the SL is a binary image calculated as

$$B_i(x,y) = \begin{cases} 1, & \text{if } F_i(x,y) > T_h \\ 0, & \text{if } F_i(x,y) < T_h \end{cases} \tag{3}$$

where $i = [1, N]$, F_i is the feature (e.g., DR_{VV}) evaluated for scene i, $i = 1$ is the earliest image, $i = N$ is the most recent, and (x, y) is the spatial position in the scene. Furthermore, the SL is calculated as

$$\mathrm{SL}_i(x,y) = \begin{cases} B_i(x,y), & i = 1 \\ \alpha B_i(x,y) + (1-\alpha) SL_{i-1}(x,y), & i > 1 \end{cases} \tag{4}$$

where $i = [1, N]$. SL_i is the level of stability measured at scene i. The coefficient α is the level of weighting, which is defined between 0 and 1. A high α discounts older observations faster, and for $\alpha = 1$, $\mathrm{SL}_i(x, y) = B_i(x, y)$, i.e., equal to the current binary image i. For $\alpha = 0$, $\mathrm{SL}_i(x, y) = B_1(x, y)$, i.e., all new observations are discarded. Hence, in order to include and weight all scenes in a time series, α cannot be 0 or 1.

The choice of α is somewhat arbitrary, but in this work, α was set to 0.5. This gives the current observation equal weight to that of all previous observations combined. Maps of SL show the most recent measurement, i.e., SL_N. In order to obtain a realistic SL map, the total number of scenes must exceed 2 and $\alpha \in (0, 1)$; otherwise, the SL is only a binary image. The values from the weighted running average filter are then scaled between 0% and 100% so that a value of 100% indicates completely stable oil pixels, i.e., the feature value for a given pixel location is always above T_h throughout the time series. The choice of T_h is tunable to cover the range of values within the scene, with high values of T_h used to identify the high-damping-ratio areas as a proxy for slick thickness. The benefits of using the weighted running average filter implemented in the SL are that the weights are independent of the number of scenes available, and we can update the SL map whenever a new acquisition is obtained. To reduce radar speckle while preserving the spatial resolution, in this study, $\mathrm{DR}_{\mathrm{VV}}$ is smoothed with a 5×5 moving average mask prior to the calculation of the SL.

B. Method 2—Radiometric Change Detection for Identifying Drift Patterns

Method 2 investigates the change in the polarimetric information as a function of both time and space to create a map that can be used to understand short-term drift patterns. Change detection using SAR images have been widely explored for various applications such as monitoring vegetation, urban, and agricultural areas. The surfaces of the clean sea and the oil slicks are highly nonstationary, and due to the dynamic changes within the slicks and the ocean, the backscattered signals vary from one acquisition to the next. Therefore, exploring changes on a pixel-to-pixel basis is inefficient. In this study, a window size of 5×5 pixels is used to obtain the local mean value from the input feature image ($\mathrm{DR}_{\mathrm{VV}}$ or CPR_c). The difference in the mean (r_{DM}) feature value is calculated between the reference flight and the other flights in the following manner:

$$r_{\mathrm{DM}} = \mu_{\mathrm{ID}} - \mu_{\text{ref. flight}} \tag{5}$$

where ID is the flight ID, μ_{ID} is the local mean within a 5×5 window from scene ID, and $\mu_{\text{ref. flight}}$ is the local mean calculated from the reference flight. If the r_{DM} is close to 0, then no change has occurred between two scenes on average within the 5×5 neighborhood. Note that this method only considers two scenes, as opposed to method 1 that incorporates information from all the scenes in the time series.

V. Results and Discussion

The two methods are applied to the three-time series (TS-1, TS-2, and TS-3) to detect the stability of the features and drift patterns of the slicks. The following sections present the results and a discussion of how the methodology can be used.

A. Method 1—Detection of Stable Regions Within the Oil Slick

The overall aim of the SL method is to locate and quantify regions that have a consistently high damping ratio over a period of time. Given that it takes time to deploy boats to a spill during clean-up operations, directing them to areas likely to have and to continue to retain thicker oil will reduce deployment time.

The range of $\mathrm{DR}_{\mathrm{VV}}$ values is approximately 1–5 for the scenes in TS-1, 1–8 for the scenes in TS-2, and 1–10 for the TS-3 scenes. Here, we calculate the SL [see (4)] using in total six scenes (the latest scenes) in each time series, to enable the same number of scenes with equal time difference between scene for comparison. The results of this procedure are shown in Fig. 6.

The different maps in Fig. 6 show the SL for thresholds $T_h =$ 2, 3, and 4. Since a weighting factor of 0.5 is used [see (4)], an SL value above 50% will indicate that the latest acquisition and some scenes prior to the latest scene had a $\mathrm{DR}_{\mathrm{VV}}$ above the threshold. Furthermore, if the SL is below 50% the latest scene did not have a $\mathrm{DR}_{\mathrm{VV}}$ above the threshold, but some prior scenes did. Regions of high SL values (above 98%) are colored dark red to clearly indicate the areas that are the most stable, and Fig. 6(b), (c), (e), (f), (h), and (i) indicates regions where $\mathrm{DR}_{\mathrm{VV}}$ is relatively high (above 3) across the entire time series. Higher damping values likely indicate thicker or more emulsified oil.

For the TS-1 scenes [see Fig. 6(a)–(c)], the dark red areas become more constrained toward the southern part of the main slick (closer to the source of the seep) when the threshold of $\mathrm{DR}_{\mathrm{VV}}$ increases. When a threshold of 4 is used, three main regions show 100% stability (dark red) in TS-2 scenes [see Fig. 6(d)–(f)], e.g., the slick in B_1 shows a stable region stretching from south to north. One small area on the southeast side of B_1 has a 100% stability. The oil slick in B_3 also shows an area of high SL over the 2-h time period. The oil slick located in B_3 has been on the surface longer compared to the oil slick in B_1 and B_2. Potential reasons for having these high damping ratio values in B_3 are emulsification [37] and/or oil accumulation in the river-induced front from the plume river dynamics of the Mississippi River [14]. There is a high SL area in C_1. The elongated oil slick area in C_2 also has a stable region of high $\mathrm{DR}_{\mathrm{VV}}$ values [above 4; see Fig. 6(i)]. This is of special importance since this slick region has been subject to weathering for a longer time period compared to the southeast part of the slick, closest to the source. The high $\mathrm{DR}_{\mathrm{VV}}$ value might be a result of the formation of emulsions over time [37] or of accumulation of oil along the fronts.

Method 1 does not account for the direction in which the thick oil is being transported by winds and currents, which is considered by method 2.

B. Method 2—Radiometric Change Detection for Identifying Drift Patterns

Prior work combining short SAR time series of slick evolution with oil drift modeling showed that both wind and local currents can significantly affect short term drift patterns [38]–[40]. In coastal areas where the currents can change over short spatial scales, accurately modeling drift patterns is challenging. Method 2 calculates the difference in the local mean feature values (r_{DM}) between two scenes to identify drift patterns independent of modeling or knowledge of local currents and wind. Method 2 is applied on TS-2 and TS-3 (see Figs. 7 and 9). Similar results apply for TS-1 (not shown).

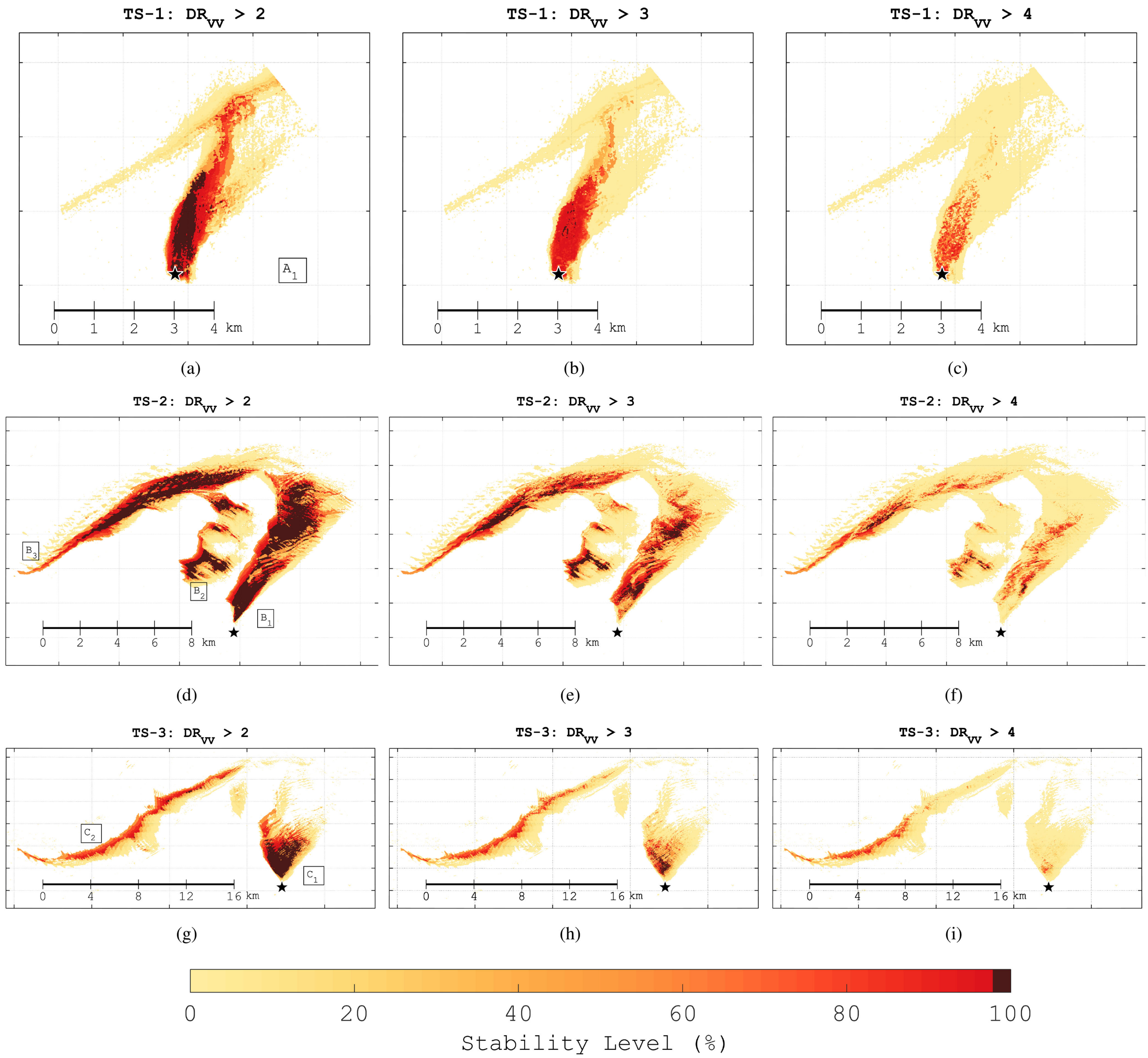

Fig. 6. Maps showing the SL in percent of $\mathrm{DR_{VV}}$ for various values of T_h. (a)–(c) SL extracted from the TS-1 scenes. (d)–(f) SL maps from the TS-2 scenes. (g)–(i) SL maps from the TS-3 scenes. The black star is the approximate location of the seep (see, e.g., [11] and [14]).

Information about persistent areas (being the same media, either oil or clean sea, in the two scenes) and areas in transitions are shown in Figs. 7(a)–(c) and 9(a)–(c) and are generated by change detection based on the oil slick masks obtained from segmentation. The light red and blue colors correspond to areas that are persistent, while the dark red and blue colors show areas in transition between oil-coverage and clean sea or vice versa. This is considered as the ground truth, and comparison to these maps is discussed in the upcoming paragraphs.

Figs. 7(d)–(f) and 9(d)–(f) show the r_{DM} obtained using $\mathrm{DR_{VV}}$ with the first flight in the given time series as the reference flight. The orange-red areas indicate where $\mathrm{DR_{VV}}$ has increased in value from the first flight, while yellow colors indicate little change between the first flight to the flight ID investigated. Green–blue indicates areas where there has been a decrease in $\mathrm{DR_{VV}}$. Figs. 7(g)–(i) and 9(g)–(i) show r_{DM} using CPR_c, where a similar interpretation applies. Note that the colorbar is reversed for CPR_c compared to the colorbar used for $\mathrm{DR_{VV}}$ because oil causes a lower CPR_c value compared to clean sea, which is the opposite trend from that of $\mathrm{DR_{VV}}$. There are several possible r_{DM} images that could be displayed, but only three of them are shown in Figs. 7 and 9. Fig. 8 shows results of thresholding $r_{\mathrm{DM}}(\mathrm{DR_{VV}})$, which are compared to Fig. 7(c).

1) Discussion of the Short-Term Drift Pattern of TS-2: A clear oil drift pattern is observed within the three areas B_1, B_2, and B_3 (see Fig. 7). In general, the oil in B_1 and B_2 spreads out in the northwest direction, while the oil in B_3 moves in the southwest direction. The oil slick in B_1 is closest to the source of the oil (black star in Fig. 7). The red/orange band on the western part of B_1 in Fig. 7(d)–(i) indicates an increase (decrease) in

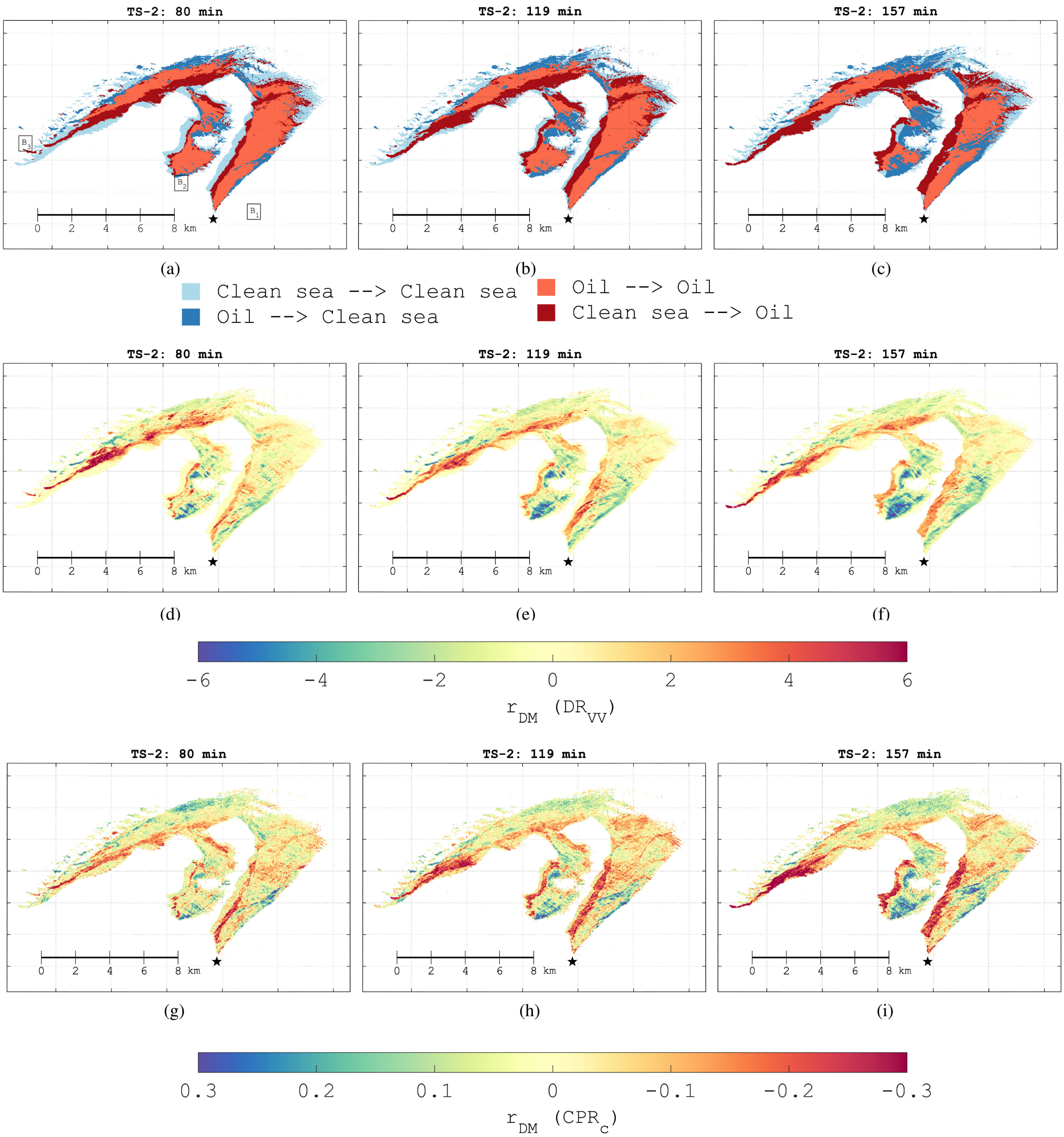

Fig. 7. (a)–(c) Maps (based on the oil slick masks) showing the persistent areas colored light blue for clean sea and light red for oil. The areas in transition are colored dark blue or dark red for "oil→ clean sea" or "clean sea→ oil," respectively. The time (min) given in the header of each map represents time since the first acquisition, i.e., the reference flight ID 000. (d)–(f) Maps showing the local mean difference (r_{DM}) of $\mathrm{DR}_{\mathrm{VV}}$ between flight ID 000 and some of the other flights. The colors range from blue indicating a decrease in $\mathrm{DR}_{\mathrm{VV}}$ to red indicating an increase in $\mathrm{DR}_{\mathrm{VV}}$. (g)–(i) Maps showing r_{DM} of CPR_c between flight ID 000 and some of the other flights. The colors range from red indicating a decrease in CPR_c, to blue indicating an increase in CPR_c. The black star is the approximate location of the persistent seep in MC-20.

$\mathrm{DR}_{\mathrm{VV}}$ (CPR_c). This red/orange band gets wider with time, indicating that the oil spreads out in the northwest direction, which is in accordance with the wind direction. However, on the east side of B_1, $\mathrm{DR}_{\mathrm{VV}}$ values decrease as a function of time, which might indicate that the oil is transported from the east (blue) to the west (red) regions. The same conclusion can be drawn from CPR_c. As pointed out in [11], there is a convergence zone entering from the east side of B_1 at approximately 80 min after the first acquisition and moves northwards throughout the time series. The oil slick in B_3 is located where the near-shore coastal current has a southwestern direction, as opposed to the slick in B_1 and B_2 where the ocean current is toward the northeast [16]. In B_3, the oil is transported with the coastal current toward the southwest, and not with the wind as the oil in B_1 and B_2. Again, for the oil slick in B_3, there are decreasing $\mathrm{DR}_{\mathrm{VV}}$ values on the opposite side from where there is an increase, indicating

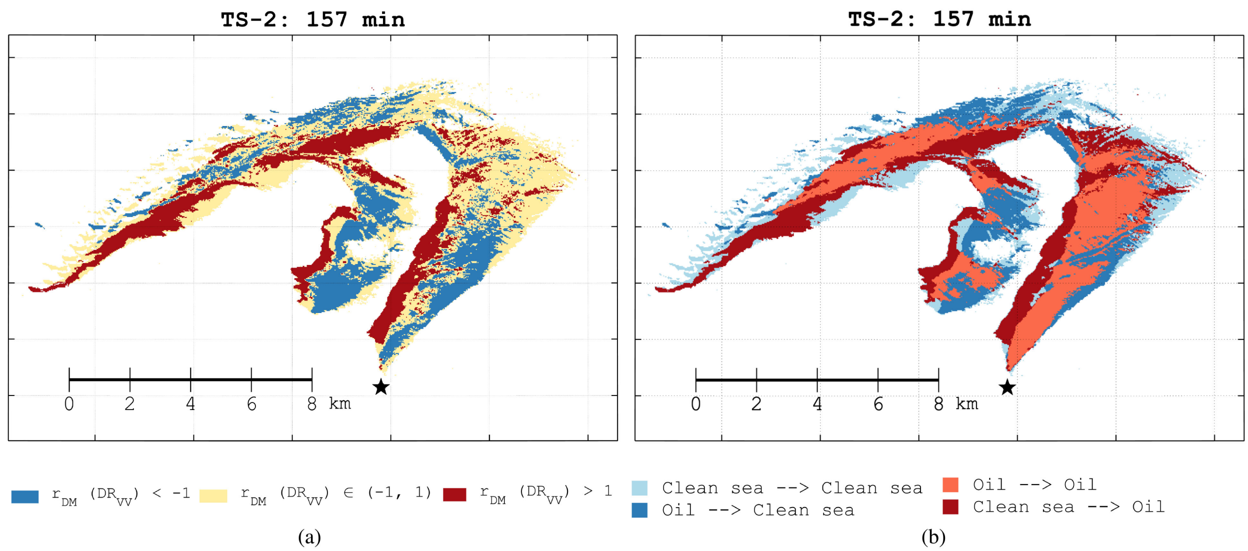

Fig. 8. (a) Map based on thresholding of $r_{\mathrm{DM}}(\mathrm{DR_{VV}})$ between the first acquisition and the last acquisition (157-min difference), i.e., thresholding of Fig. 7(f). (b) Fig. 7(c) is repeated for easier comparison.

oil movement. In general, r_{DM} using CPR_c [see Fig. 7(g)-(i)] shows a similar behavior as r_{DM} for $\mathrm{DR_{VV}}$ [see Fig. 7(d)–(f)]. $\mathrm{DR_{VV}}$ and CPR_c are similar for B_1 and B_2, where r_{DM} from CPR_c also captured the spreading of the oil.

2) Comparison of Figs. 7(c) and 8 for TS-2: Fig. 8(a) shows thresholding of $r_{\mathrm{DM}}(\mathrm{DR_{VV}})$ of Fig. 7(f), and Fig. 8(b) shows the same map in Fig. 7(c) for easier comparison. The dark blue areas in Fig. 8(a) indicate a decrease larger than 1 for $\mathrm{DR_{VV}}$ between the first and last acquisition in TS-2 [see Fig. 7(f)]. A decrease in $\mathrm{DR_{VV}}$ with time corresponds to when oil was present in the first acquisition, but not in the last acquisition. An alternative explanation is a decrease in the oil concentration or thickness layers between the two scenes, since a large part of the area shown was in category "oil→ oil" [light red color in Fig. 8(b)], meaning that oil was present for the entire time interval, but a decrease in $\mathrm{DR_{VV}}$ occurred. Furthermore, the dark red area in Fig. 8(a) corresponds well with the dark red area in Fig. 8(b), indicating an increase in $\mathrm{DR_{VV}}$ above 1 between the two scenes, which corresponds to oil drifting/spreading into these areas during the 157-min time interval. Overall, the primary differences between Fig. 8(a) and (b) are between the yellow areas [see Fig. 8(a)], which corresponds mostly to the light red and light blue areas in Fig. 8(b). This difference is due to $\mathrm{DR_{VV}}$ only decreasing slightly [changes in the range from -1 to 1; see yellow-colored areas in Fig. 8(a)] over the 157-min time interval. Similar figures and interpretation applies for TS-3, but are not shown here.

3) Discussion of the Short-Term Drift Pattern of TS-3: Fig. 9(d)–(f) shows r_{DM} based on $\mathrm{DR_{VV}}$ for the TS-3 scenes, whereas Fig. 9(g)–(h) shows r_{DM} based on CPR_c. The effect of the wind can clearly be seen for the oil slick in C_1, where $\mathrm{DR_{VV}}$ increases on the western part of C_1 and decreases on the eastern part of C_1. This is a result of the oil being transported from east to west by the wind. The same phenomena are observed for CPR_c. For the oil slick in C_2, the effect of both the wind and the southwestern ocean current is present. First, the wind pushes the oil in the northwest direction, which can be seen by the red region being located above the blue-colored region in Fig. 9(d)–(i). This is also seen in Fig. 9(a)–(c), where the red band (clean sea→ oil) is above the dark blue area (oil→ clean sea). In the south of the red band in C_2, there is a corresponding blue band that also gets wider with time, which reveals that $\mathrm{DR_{VV}}$ decreases and CPR_c increases as the slick moves out of this area. Having similar observations of r_{DM} for both $\mathrm{DR_{VV}}$ and CPR_c might indicate an increase in the oil concentration, which could be a result of accumulation of oil due to the wind drag (most likely) and/or the riverfront, or to oil emulsification. The oil at the surface might also initially be fairly thick/concentrated and then spreads out as sheen by winds and currents and be pushed against the plume resulting in accumulation of oil along the fronts.

C. Limitations

One of the drawbacks of method 1 (SL) is the need for tuning T_h, but for these three-time series, a threshold of 3 was able to capture patches of oil with high damping ratio values over a period of time. However, this threshold might differ from other oil types, sensors, and metocean conditions and should only be tuned within each time series. The damping ratio is also sensitive to wind and sea state conditions, and at high wind speed, the damping ratio is expected to be smaller than at low-to-moderate wind speeds (4–7 m/s) [3]. This might impact the threshold that is used. The wind speed was measured to be between 3.8 and 6.6 m/s for the two days, which indicates comparable conditions. It is recommended that additional tests for other sea state and weather conditions be performed in future work.

Furthermore, the two methods can only be applied using short-term time series, since a time series spanning many days might cover various sea and wind states, which could influence the damping ratio values and the threshold in method 1. As mentioned in the previous section, the goal of the two methods is to demonstrate that change detection can be performed on

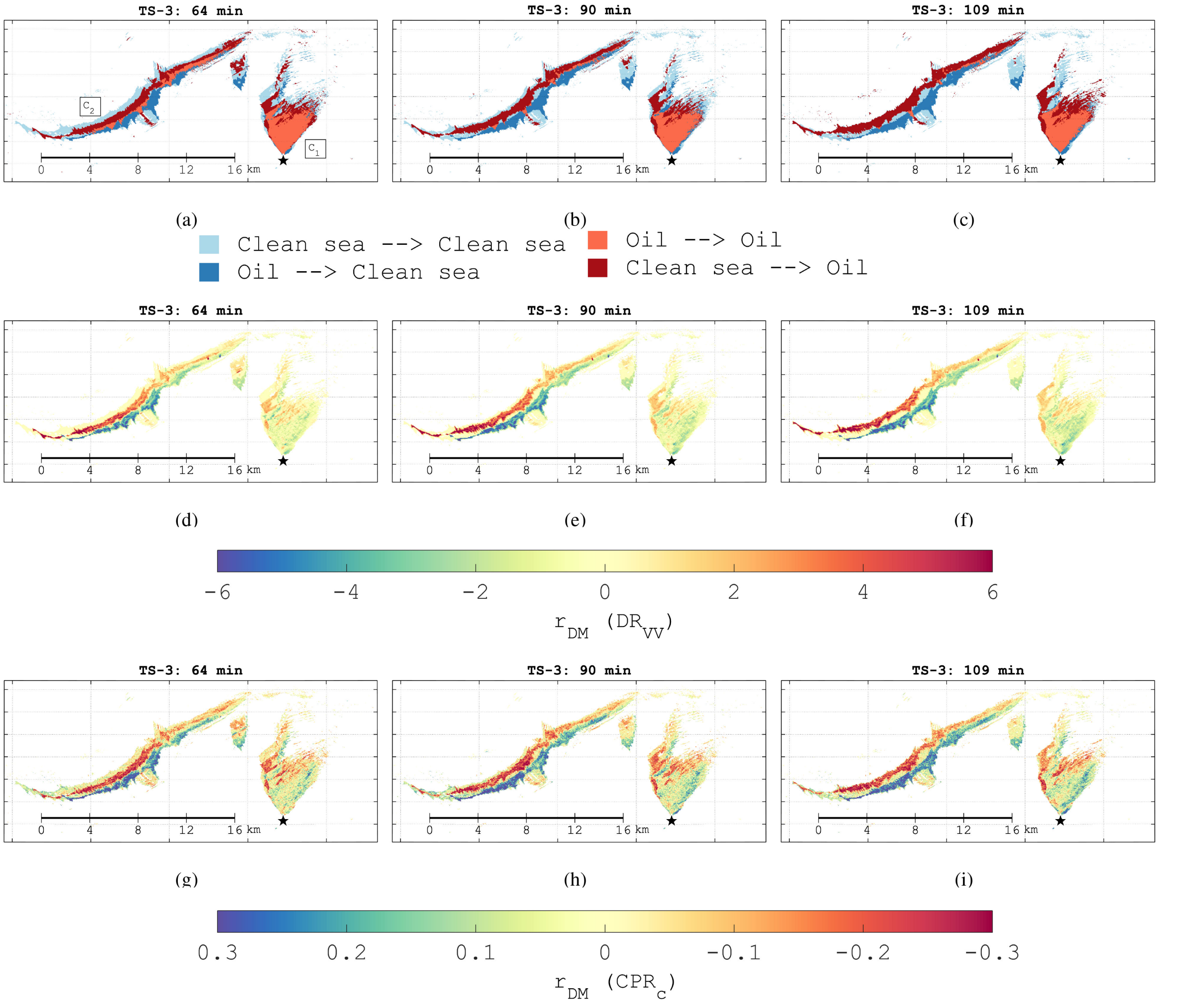

Fig. 9. (a)–(c) Maps (based on the oil slick masks) showing the persistent areas colored light blue for clean sea and light red for oil. The areas in transition are colored dark blue or dark red for "oil→ clean sea" or "clean sea→ oil," respectively. The time (min) given in the header of each map represents time since the first acquisition, i.e., the reference flight ID 000. (d)–(f) Maps showing the local mean difference (r_{DM}) of $\mathrm{DR}_{\mathrm{VV}}$ between flight ID 000 and some of the other flights. The colors range from blue indicating a decrease in $\mathrm{DR}_{\mathrm{VV}}$ to red indicating an increase in $\mathrm{DR}_{\mathrm{VV}}$. (g)–(i) Maps showing r_{DM} of CPR_c between flight ID 000 and some of the other flights. The colors range from red indicating a decrease in CPR_c, to blue indicating an increase in CPR_c. The black star is the approximate location of the persistent seep in MC-20.

a short time scale. Another limitation of both methods is that a clean sea region needs to be present in the SAR scene when calculating $\mathrm{DR}_{\mathrm{VV}}$, but given the size of scenes from most remote sensing instruments, this is commonly not a limiting factor. The results are obtained under moderate wind conditions, and further research regarding other metocean conditions is necessary. Further testing is still required to confirm the relationship between relative oil thickness and damping ratio ($\mathrm{DR}_{\mathrm{VV}}$).

D. *Summary*

Figs. 10 and 11 show close-up images of $\mathrm{DR}_{\mathrm{VV}}$ [see Figs. 10(a) and 11(a)], SL (when $\mathrm{DR}_{\mathrm{VV}} > 3$) [see Figs. 10(b) and 11(b)], and r_{DM} (using $\mathrm{DR}_{\mathrm{VV}}$) [see Fig. 10(c) and 11(c)] for the region closest to the source of the seep, i.e., southern part of B_1 (TS-2) and C_1 (TS-3). Figs. 10(a) and 11(a) show the last $\mathrm{DR}_{\mathrm{VV}}$ image in the time series, in which variation of the oil characteristics with the slick is evident. The areas with high $\mathrm{DR}_{\mathrm{VV}}$ values in the most recent image should be prioritized, but these areas do not hold information about the past, which the SL image provides. For comparison, the darkest red areas in SL [see Figs. 10(b) and 11(b)] are where $\mathrm{DR}_{\mathrm{VV}} > 3$ in all the scenes of the time series. Therefore, SL shows both where the thicker oil was most recently (values $\geqq$ 50%) and where the oil has persistently been in a particular area (values approaching 100%). The SL map clearly locates the persistent high damping ratio areas within the slick. The dark red regions should, therefore, be prioritized as good starting points for the recovery operation.

Figs. 10(c) and 11(c) show where the oil is spreading/drifting based on the r_{DM} calculated with $\mathrm{DR}_{\mathrm{VV}}$. The oil slicks in both Figs. 10 and 11 are spreading toward the northwest. Having this information available could aid in navigating into the site and

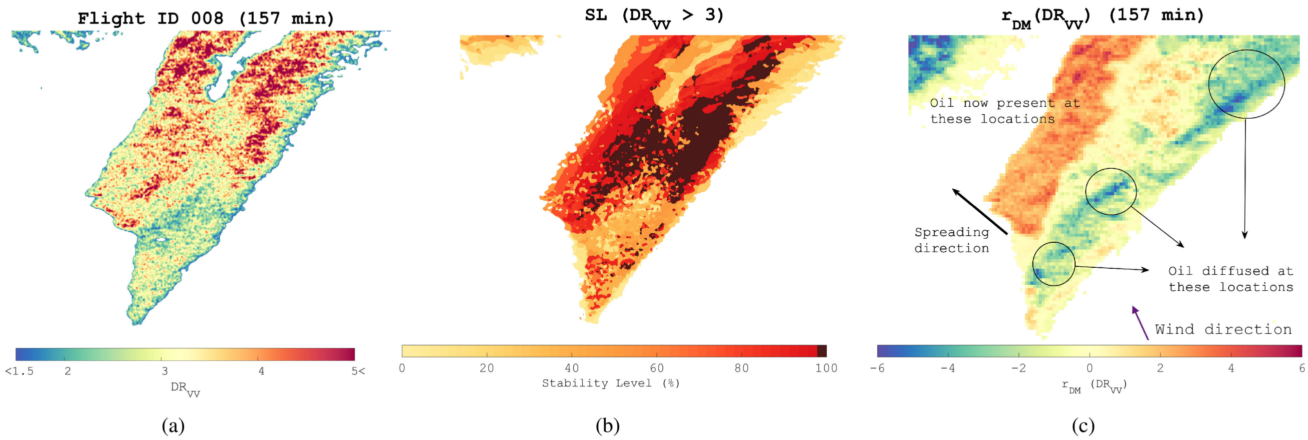

Fig. 10. (a) Detailed DR_{VV} image of the lower part of B_1 from TS-2. (b) SL from the last scene in the time series [see Fig. 6(e)]. (c) Mean difference of DR_{VV} between the first and last scenes in TS-2 [see Fig. 7(f)]. The time (in min) since the first acquisition is shown in the header of (a) and (c).

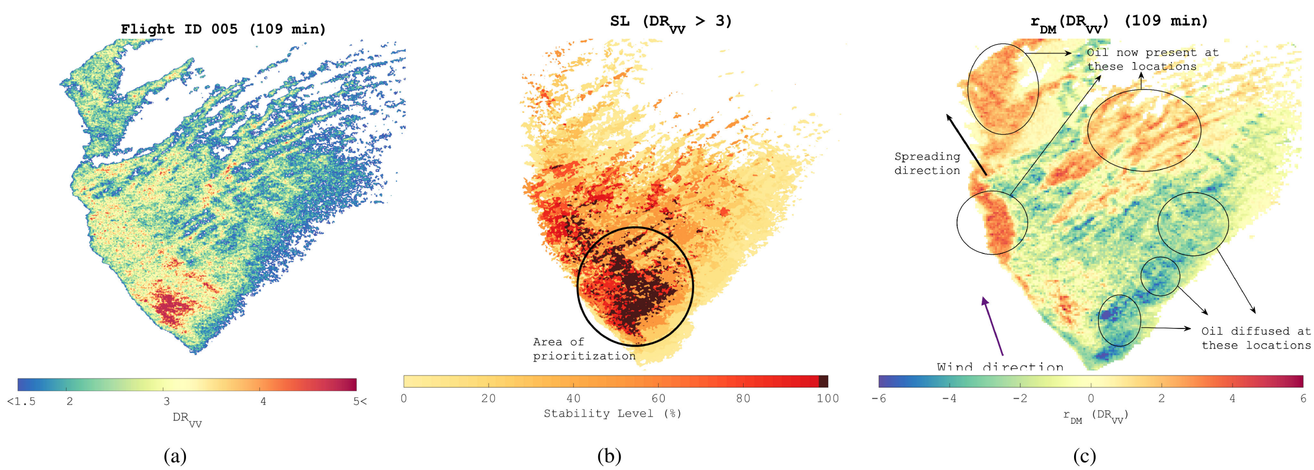

Fig. 11. (a) Detailed DR_{VV} image of the lower part of C_1 from TS-3. (b) SL from the last scene in the time series [see Fig. 6(e)]. (c) Mean difference of DR_{VV} between the first and last scenes in TS-2 [see Fig. 7(f)]. The time (in min) since the first acquisition is shown in the header of (a) and (c).

planning the timeline for recovery and use of field resources. The SL and r_{DM} maps provide complementary information to the single DR_{VV} image in a given time series.

VI. Conclusion

The overall goal of this study is to demonstrate two complementary semiautomated methods that can be used with time-series data to produce maps showing the trends in slick transport and weathering without requiring visual inspection of each of the scenes, while also incorporating a memory of the evolution history. Two methods, SL and r_{DM}, are suggested, which are complementary in terms of identifying the zones of stability within a slick, the drift patterns of the slick, and the weathering and accumulation of oil to form higher damping surface layers. These are important aspects in the planning and execution of a clean-up process. The methods are summarized as follows.

Method 1: This method is used to identify patches within the slick that consistently exhibit a high damping ratio over a period of time, assumed to indicate thicker oil. The information obtained from the SL can be used in an oil spill recovery operation, where high SL areas should be investigated first, and to direct crews to the site since deployment from base could take a while, in particular in remote locations such as in the Arctic. It is only reasonable to use the SL method over a short time period as the oil slick might drift sufficiently far that the slick masks are nonoverlapping. Additionally, this method could also be well suited to obtain an overview of a persistent leak from platforms or pipelines. In the scenario studied here, the oil originates from a seep at the seafloor, and new oil is continuously emerging at the surface. Hence, the SL method is suited for this type of scenario, and the high SL values could be of special importance as they reveal patches of high damping ratio over a longer period of time. Further studies should be conducted on oil slicks that are spilled at the surface and not leaked from the seabed as in this case.

Method 2: The SL method detects regions of consistently high DR_{VV} values, but it cannot detect where the oil is moving. The second method compliments this by obtaining an overview of the oil drift pattern using the mean change (r_{DM}) of both DR_{VV} and CPR_c and the difference in the oil masks between two scenes. Here, both information about the oil movement and the backscatter change within the oil slick can be obtained. $\mathrm{DR}_{\mathrm{VV}}$ and CPR_c demonstrated similar results in r_{DM}. $\mathrm{DR}_{\mathrm{VV}}$ can, thus, be recommended, since only one polarization channel is needed to identify variations within the slick. Another goal of this method was to identify areas that the oil is moving to and from, i.e., small-scale drift patterns.

Scene-to-scene changes using airborne SAR need to be restricted to the actual backscatter properties of the target. These changes are the different sensor properties, such as imaging geometry (look direction and incidence angle), frequency, polarization, resolution, and swath width, which are likely to impact the scene to scene variations, so these should be unchanged during the airborne acquisitions. A recent development is the introduction of cost-effective SAR microsatellites.[4] The increasing number of such affordable satellites may in the future enable multiple observations on a daily basis without the use of an aircraft. Combining such microsatellites and other spaceborne satellites, it might be possible to construct a time series of spaceborne SAR images with short time difference between scenes. However, the different sensor properties could obfuscate the observed changes on the surface between scenes, which must be considered in a time series analysis. Due to the simplicity of the two methods presented, they could be adapted to other sensor types, such as optical satellites, but using other input features.

Acknowledgment

The authors would like to thank the Jet Propulsion Laboratory (JPL) National Aeronautics and Space Administration team for the collection of the UAVSAR and *in situ* data. The authors would also like to thank Wenqing Tang at JPL for providing the algorithm for converting to equivalent neutral wind. UAVSAR data can be downloaded from the Alaska Satellite Facility (www.asf.alaska.edu). Finally, the authors would also like to thank the reviewers for all the valuable feedback that helped improve this study.

References

[1] S. Skrunes, C. Brekke, T. Eltoft, and V. Kudryavtsev, "Comparing near-coincident C- and X-band SAR acquisitions of marine oil spill," *IEEE Trans. Geosci. Remote Sens.*, vol. 53, no. 4, pp. 1958–1975, Apr. 2015.

[2] M. Gade, W. Aplers, H. Hühnerfuss, V. R. Wismann, and P. A. Langes, "On the reduction of the radar backscatter by oceanic surface Films: Scatterometer measurements and their theoretical interpretation," *Remote Sens. Environ.*, vol. 66, no. 1, pp. 52–70, Oct. 1998.

[3] M. Gade, W. Alpers, H. Hühnerfuss, H. Masuko, and T. Kobayashi, "Imaging of biogenic and anthropogenic ocean surface films by the multifrequency/multipolarization SIR-C/X-SAR," *J. Geophys. Res. Oceans*, vol. 103, no. C9, pp. 18851–18866, Aug. 1998.

[4] S. Skrunes, C. Brekke, and T. Eltoft, "Characterization of marine surface slicks by Radarsat-2 multipolarization features," *IEEE Trans. Geosci. Remote Sens.*, vol. 52, no. 9, pp. 5302–5319, Sep. 2014.

[5] B. Minchew, C. E. Jones, and B. Holt, "Polarimetric analysis of backscatter from the deepwater horizon oil spill using L-band synthetic aperture radar," *IEEE Trans. Geosci. Remote Sens.*, vol. 50, no. 10, pp. 3812–3830, Oct. 2012.

[6] B. Minchew, "Determining the mixing of oil and sea water using polarimetric synthetic aperture radar," *Geophys. Res. Lett.*, vol. 39, no. 16, Aug. 2012, Art. no. L16607.

[4]See, e.g., www.iceye.com for information regarding one of first SAR microsatellite. Last visited on March 19, 2020.

[7] M. Migliaccio, F. Nunziata, and A. Buono, "SAR polarimetry for sea oil slick observation," *Int. J. Remote Sens.*, vol. 36, no. 12, pp. 3243–3273, Jun. 2015.

[8] A.-B. Salberg, O. Rudjord, and A. H. S. Solberg, "Oil spill detection in hybrid-polarimetric SAR images," *IEEE Trans. Geosci. Remote Sens.*, vol. 52, no. 10, pp. 6521–6533, Oct. 2014.

[9] S. Angelliaume *et al.*, "SAR imagery for Detecting sea surface slicks: Performance assessment of polarization-dependent parameters," *IEEE Trans. Geosci. Remote Sens.*, vol. 56, no. 8, pp. 1–21, Aug. 2018.

[10] V. Wismann, M. Gade, W. Alpers, and H. Hühnerfuss, "Radar signatures of marine mineral oil spills measured by an airborne multi-frequency radar," *Int. J. Remote Sens.*, vol. 19, no. 18, pp. 3607–3623, Nov. 1998.

[11] C. E. Jones and B. Holt, "Experimental L-band airborne SAR for oil spill response at sea and in coastal waters," *Sensors*, vol. 18, no. 2, Feb. 2018, Art. no. 641.

[12] S. Skrunes, C. Brekke, and M. M. Espeseth, "Assessment of the RISAT-1 FRS-2 mode for oil spill observation," in *Proc. IEEE Int. Geo. Remote Sens. Symp.*, 2017, pp. 1024–1027.

[13] S. Sun, C. Hu, O. Garcia-Pineda, V. Kourafalou, M. L. Hénaff, and Y. Androulidakis, "Remote sensing assessment of oil spills near a damaged platform in the Gulf of Mexico," *Mar. Pollut. Bull.*, vol. 136, pp. 141–151, 2018.

[14] Y. Androulidakis *et al.*, "Influence of river-induced fronts on hydrocarbon transport: A multiplatform observational study," *J. Geophys. Res. Oceans*, vol. 123, no. 5, pp. 3259–3285, 2018.

[15] F. Nunziata, C. R. de Macedo, A. Buono, D. Velotto, and M. Migliaccio, "On the analysis of a time series of X-band TerraSAR-X SAR imagery over oil seepages," *Int. J. Remote Sens.*, vol. 40, no. 9, pp. 3623–3646, 2019.

[16] C. E. Jones, M. M. Espeseth, B. Holt, and C. Brekke, "Measurement of oil slick transport and evolution in the Gulf of Mexico using L-band synthetic aperture radar," in *Proc. 12th Eur. Conf. Synth. Aperture Radar*, 2018, pp. 1–5.

[17] P. C. Genovez, C. E. Jones, S. J. S. Sant'Anna, and C. C. Freitas, "Oil slick characterization using a statistical region-based classifier applied to UAVSAR data," *J. Mar. Sci. Eng.*, vol. 7, no. 2, Feb. 2019, Art. no. 36.

[18] S. Skrunes, C. Brekke, and T. Eltoft, "Oil spill characterization with multi-polarization C- and X-band SAR," *IEEE Int. Geosci. Remote Sens. Symp.*, 2012, pp. 5117–5120.

[19] B. Jones, "A comparison of visual observations of surface oil with synthetic aperture radar imagery of the sea empress oil spill," *Int. J. Remote Sens.*, vol. 22, no. 9, pp. 1619–1638, Nov. 2001.

[20] I. Sergievskaya, S. Ermakov, T. Lazareva, and J. Guo, "Damping of surface waves due to crude oil/oil emulsion films on water," *Mar. Pollut. Bull.*, vol. 146, pp. 206–214, 2019.

[21] L. Herbst, E. DeCola, and K. Kennedy, "New pathways for developing and testing oil spill response equipment in real world conditions," in *Proc. OCEANS 2016 MTS/IEEE Monterey*, 2016, pp. 1–6.

[22] C. E. Jones, M. M. Espeseth, B. Holt, C. Brekke, and S. Skrunes, "Characterization and discrimination of evolving mineral and plant oil slicks based on L-band synthetic aperture radar (SAR)," *Proc. SPIE*, vol. 10003, 2016, Art. no. 100030K.

[23] W. Alpers and H. A. Espedal, "Oils and surfactants," in *Synthetic Aperture Radar Marine User's Manual* C. R. Jackson and J. R. Apel, Eds. Silver Spring, MD, USA: NOAA/NESDIS, Sep. 2004, ch. 11, pp. 263–275.

[24] G. Franceschetti, A. Iodice, D. Riccio, G. Ruello, and R. Siviero, "SAR raw signal simulation of oil slicks in ocean environments," *IEEE Trans. Geosci. Remote Sens.*, vol. 40, no. 9, pp. 1935–1949, Sep. 2002.

[25] G. R. Valenzuela, "Theories for the interaction of electromagnetic and oceanic waves—A review," *Boundary-Layer Meteorol.*, vol. 13, nos. 1/4, pp. 61–85, Jan. 1978.

[26] S. R. Cloude, *Polarisation Applications in Remote Sensing*. New York, NY, USA: Oxford Univ. Press, 2010, pp. 125–129.

[27] A. G. Fore *et al.*, "UAVSAR polarimetric calibration," *IEEE Trans. Geosci. Remote Sens.*, vol. 53, no. 6, pp. 3481–3491, Jun. 2015.

[28] S. D. Asl, J. Amos, P. Woods, O. Garcia-Pineda, and I. R. MacDonald, "Chronic, anthropogenic hydrocarbon discharges in the Gulf of Mexico," *Deep Sea Res. Part II: Topical Stud. Oceanography*, vol. 129, pp. 187–195, 2016.

[29] R. E. Turner *et al.*, "Distribution and recovery trajectory of Macondo (Mississippi canyon 252) oil in louisiana coastal wetlands," *Mar. Pollut. Bull.*, vol. 87, no. 1, pp. 57–67, 2014.

[30] C. J. Warren, A. MacFadyen, and C. Henry, Jr., "Mapping oil for the destroyed Taylor energy site in the Gulf of Mexico," in *Proc. Int. Oil Spill Conf. Proc.*, 2014, Art. no. 299931.

[31] Ø. Johansen, H. Rye, and C. Cooper, "DeepSpill-field study of a simulated oil and gas blowout in deep water," *Spill Sci. Technol. Bull.*, vol. 8, nos. 5/6, pp. 433–443, 2003.

[32] J. Coleman, *Oil in the Sea III*. Washington DC, USA: National Acad. Press, 2003.

[33] W. T. Liu and W. Tang, "Equivalent neutral wind," Jet Propulsion Lab., Pasadena, CA, USA, JPL Publication 96-17, 1996.

[34] W. Alpers and H. Hühnerfuss, "The damping of ocean waves by surface films: A new look at an old problem," *J. Geophys. Res. Oceans*, vol. 94, no. C5, pp. 6251–6265, May 1989.

[35] K. P. Singh, A. L. Gray, R. K. Hawkins, and R. A. O'Neil, "The influence of surface oil on C-and Ku-band ocean backscatter," *IEEE Trans. Geosci. Remote Sens.*, vol. GE-24, no. 5, pp. 738–744, Sep. 1986.

[36] A. P. Doulgeris and T. Eltoft, "Scale mixture of Gaussian modelling of polarimetric SAR data," *EURASIP J. Adv. Signal Process.*, vol. 2010, no. 8, 2009, Art. no. 874592.

[37] M. Fingas and B. Fieldhouse, "Studies on water-in-oil products from crude oils and petroleum products," *Mar. Pollut. Bull.*, vol. 64, no. 2, pp. 272–283, Feb. 2012.

[38] H. A. Espedal, "Satellite SAR oil spill detection using wind history information," *Int. J. Remote Sens.*, vol. 20, no. 1, pp. 49–65, 1999.

[39] C. E. Jones *et al.*, "Measurement and modeling of oil slick transport," *J. Geophys. Res. Oceans*, vol. 121, no. 10, pp. 7759–7775, Nov. 2016.

[40] J. Röhrs *et al.*, "The effect of vertical mixing on the horizontal drift of oil spills," *Ocean Sci.*, vol. 14, no. 6, pp. 1581–1601, 2018.

Martine M. Espeseth received the M.Sc. and Ph.D. degrees in remote sensing from the Department of Physics and Technology, UiT The Arctic University of Norway, Tromsø, Norway, in 2015 and 2019, respectively.

She is currently a Postdoctoral Researcher with the Department of Physics and Technology, Centre for Integrated Remote Sensing and Forecasting for Arctic Operations, UiT The Arctic University of Norway. From February 2016 to April 2016 and August 2018 to December 2018, she was a visiting Ph.D. student with the Jet Propulsion Laboratory, California Institute of Technology, Pasadena, CA, USA. Her current research interests include remote sensing of polarimetric synthetic aperture radar, with a focus on compact polarimetry within both marine oil pollution and sea ice applications.

Cathleen E. Jones (Member, IEEE) received the B.S. degree from Texas A&M University, College Station, TX, USA, in 1982, and the Ph.D. degree from the California Institute of Technology, Pasadena, CA, USA, in 1991, both in physics.

She is currently a Radar Scientist with NASA's Jet Propulsion Laboratory, California Institute of Technology, where her main research is focused on using radar remote sensing for studying natural disasters and monitoring critical infrastructure, primarily using high-resolution L-band polarimetric synthetic aperture radar (SAR), and interferometric synthetic aperture radar (InSAR) based on uninhabited aerial vehicle SAR data. In addition, she has done work detecting sinkhole precursor in InSAR-challenged areas. Her research interests include development of methods for determining oil slick characteristics and identifying levee deformation, seepage, and general subsidence rates using SAR.

Benjamin Holt (Member, IEEE) received the B.S. degree from Stanford University, Stanford, CA, USA, in 1972, and the M.S. degree in physical oceanography from the University of Southern California, Los Angeles, CA, in 1988.

In 1978, he joined the Ocean Circulation Group, Earth Science Section, Jet Propulsion Laboratory, California Institute of Technology, Pasadena, CA, as a Research Scientist.. His research interests include using multisensor remote sensing data to examine the geophysical state of polar sea ice and snow, coastal oceanography and circulation, and the detection of marine pollutants. In addition, he is also involved with new instrument development and techniques for microwave measurement of sea ice thickness.

Camilla Brekke (Member, IEEE) received the Cand. Mag., Cand. Scient., and Ph.D. degrees from the Department of Informatics, University of Oslo, Oslo, Norway, in 1998, 2001, and 2008, respectively.

She is currently the Vice-Dean Research with the Faculty of Science and Technology, the Deputy Centre Leader with the Centre for Integrated Remote Sensing and Forecasting for Arctic Operations and full Professor at Department of Physics and Technology, UiT The Arctic University of Norway, Tromsø, Norway. Her current research interests include synthetic aperture radar and ocean color remote sensing for arctic and marine applications.

Stine Skrunes (Member, IEEE) received the M.Sc. and Ph.D. degrees in remote sensing from the Department of Physics and Technology, UiT The Arctic University of Norway, Tromsø, Norway, in 2011 and 2014, respectively.

She is currently a Postdoctoral Researcher with the Department of Physics and Technology, with the Centre for Integrated Remote Sensing and Forecasting for Arctic Operations, UiT The Arctic University of Norway. Her current research interests include remote sensing of ocean areas, specifically by polarimetric synthetic aperture radar with a focus on marine oil pollution.